Monthly Notices of the ROYAL ASTRONOMICAL SOCIETY

MNRAS **527,** 7111–7120 (2024) https://doi.org/10.1093/mnras/stad3619
Advance Access publication 2023 November 24

New evidence of multiple channels for the origin of gamma-ray bursts with extended emission

Q. M. Li,[1] Q. B. Sun ,[2★] Z. B Zhang,[1★] K. J. Zhang[1] and G. Long[2]
[1]*Department of Physics, College of Physics, Guizhou University, Guiyang 550025, China*
[2]*Yunnan Observatories, Chinese Academy of Sciences, Kunming 650216, China*

Accepted 2023 November 21. Received 2023 November 12; in original form 2023 July 17

ABSTRACT

Gamma-ray bursts (GRBs) are the most intense explosions in the Universe. GRBs with extended emission (GRBs EE) constitute a small subclass of GRBs. GRBs EE are divided into EE-I GRBs and EE-II GRBs, according to the Amati empirical relationship rather than duration. We test here if these two types of GRB have different origins based on their luminosity function (and formation rate). Therefore, we use Lynden-Bell's c^- method to investigate the luminosity function and formation rate of GRBs with EE without any assumption. We calculate the formation rate of two types of GRBs. For EE-I GRBs, the fitting function can be written as $\rho(z) \propto (1+z)^{-0.34\pm0.04}$ for $z < 2.39$ and $\rho(z) \propto (1+z)^{-2.34\pm0.24}$ for $z > 2.39$. The formation rate of EE-II can describe as $\rho(z) \propto (1+z)^{-1.05\pm1.10}$ for $z < 0.43$ and $\rho(z) \propto (1+z)^{-8.44\pm1.10}$ for $z > 0.43$. The local formation rate is $\rho(0) = 0.03\,\mathrm{Gpc^{-3}\,yr^{-1}}$ for some EE-I GRBs and $\rho(0) = 0.32\,\mathrm{Gpc^{-3}\,yr^{-1}}$ for EE-II GRBs. Based on these results, we provide new evidence that the origins of EE-I GRBs are different from EE-II GRBs from the perspective of event rate. The EE-I GRB could be produced from the death of the massive star, but EE-II GRB may come from other processes that are unrelated to the star formation rate. Our findings indicate that the GRBs with EE could have multiple production channels.

Key words: methods: statistical – stars: formation – gamma-ray burst: general.

1 INTRODUCTION

Gamma-ray bursts (GRBs) are the most violent explosions in the universe and emit high-energy radiations that are produced in an ultrarelativistic jet (Zhang 2007; Gehrels, Ramirez-Ruiz & Fox 2009). In the internal shock model, the inner engine will produce shells with comparable energy but different Lorentz factors Γ. The slower shell, which is followed by a faster shell, catches up with it and collides, which can produce the pulse profile observable in most GRBs (Kobayashi, Piran & Sari 1997; Daigne & Mochkovitch 1998; Piran 1999). Traditionally, GRBs are divided into long GRBs (lGRBs; $T_{90} > 2$ s) and short GRBs (sGRBs; $T_{90} < 2$ s; Kouveliotou et al. 1993). T_{90} is the time interval during which the integrated photon counts accumulate from 5 per cent to 95 per cent of the total photon counts in the prompt emission. The measurement of T_{90} is influenced by different instruments. The dividing line of *Swift* GRB is 1 s (Zhang et al. 2020b; Deng et al. 2022) that is very close to the 1.27 s value of the Gamma-ray Burst Monitor (GBM) GRBs (Gruber et al. 2014), and the duration distribution peak at 0.21 and 42.66 for sGRB and lGRB, respectively. lGRBs are generally believed to originate from the death of massive stars. The association between GRB and supernovae provided direct evidence (Hjorth et al. 2003; Stanek et al. 2003). Therefore, lGRBs can be seen as a tool for tracking the star formation rate (SFR; Yu et al. 2015; Pescalli et al. 2016; Dong et al. 2022). sGRBs are believed to originate from the merger of binary compact objects. The association of sGRB 170817A with transient gravitational waves supports the idea that some sGRB is produced by binary neutron stars (BNS) system (GW 170817; Abbott et al. 2017). The more comparison of comprehensive properties of GRB associated with supernovae–kilonovae can be found in our recent work (Li et al. 2023).

However, many authors have also reported a special class of GRBs with extended emission (EE), where the EE is defined as a low-intensity burst following the initial main emission (Lazzati, Ramirez-Ruiz & Ghisellini 2001; Connaughton 2002; Burrows et al. 2005; Norris & Bonnell 2006; Lan et al. 2020). Currently, there are several popular speculations about the production of EE: (1) spin-down of a strongly magnetized neutron star (Bucciantini et al. 2012); (2) a relativistic wind extracting the rotational energy from a protomagnetar (Metzger, Quataert & Thompson 2008); and (3) material fallback of the material heated by r-process (Desai, Metzger & Foucart 2019). Current research shows that the second peak of GRB 000727 occurs 7 s after the initial peak (Mazets et al. 2002). Interestingly, EE components can be identified in both lGRBs and sGRBs from the light curve of prompt emission. Norris, Marani & Bonnell (2000) suggested an anticorrelation between spectral lag and peak luminosity for lGRB, but this relationship is different for sGRB and lGRB. Gehrels et al. (2006) found that the lag and luminosity of GRB 060614 with EE belong to the sGRB plane. Recently, the lGRB 211211A was characterized by a main emission (ME) phase (13 s) and an EE phase lasting 55 s (Rastinejad et al. 2022; Yang et al. 2022; Chang et al. 2023).

★ E-mail: sunqibin@ynao.ac.cn (Q. B.Sun); zbzhang@gzu.edu.cn (Z.B.Z)

The existence of EE makes it confusing to distinguish between lGRB and sGRB by relying only on the criterion of T_{90}. There is a general method involving the peak energy in the rest frame $E_{\rm p,\,i}$ and isotropic energy $E_{\rm iso}$, named as Amati correlation (Amati et al. 2002; Amati 2005), which is used to classify different types of GRBs (van Putten et al. 2014; Zhang et al. 2018; Minaev & Pozanenko 2020; Li et al. 2023; Zhu et al. 2023). Qin & Chen (2013) investigated the distribution of the logarithmic deviation of the peak energy in rest frame ($E_{\rm p,\,i}$). They proposed a statistical classification of GRBs in the $E_{\rm p,\,i}$ versus $E_{\rm iso}$ plane (Amati GRBs and non-Amati GRBs), in which the Amati-type bursts well follow the Amati relation, non-Amati-type bursts do not. Zhang et al. (2020a) divided lGRB/sGRB with EE into two subclasses (EE-I and EE-II) again based on their positions in the $E_{\rm p,\,i}$–$E_{\rm iso}$ plane, and suggested that these two subclasses have different origins by comparing the empirical relationship (e.g. Yonetoku correlation and peak energy distribution, etc.). According to their results, it is more reasonable to classify GRB with EE into types I and II, which motivates us to investigate their progenitors further.

It is acceptable that lGRBs are associated with the deaths of massive stars. Therefore, it is reasonable to use lGRBs to investigate the SFR (Yonetoku et al. 2004; Wang & Dai 2009; Butler, Bloom & Poznanski 2010; Yu et al. 2015). The sGRB is thought to be produced from a coalescence of compact objects. Yonetoku et al. (2014) pointed out that the key to confirming this idea is the formation rate (FR) of sGRB. Theoretically, the sGRB FR will track the SFR with some delay time. The methods to estimate the coalescence rates of binary compact object systems have large difficulties and uncertainties (Lipunov et al. 1995; Fryer, Woosley & Hartmann 1999; Belczynski, Kalogera & Bulik 2002). If sGRBs are expected to be accompanied by gravitational wave emission (e.g. GW 170817 and sGRB 170817A; Abramovici et al. 1992; Narayan, Paczynski & Piran 1992; Rossi et al. 2018), then the local sGRB FR is directly related to the expected number of gravitational wave events in the future. The FR of sGRB has been extensively explored in previous research (Ando 2004; Zhang & Wang 2018; Dainotti, Petrosian & Bowden 2021). Two of the critical properties characterizing the population of GRBs are their FR and luminosity function (LF), which are helpful to profoundly understand the nature of GRBs (Dermer 2007; Pescalli et al. 2016). FR and LF, respectively, represent the number of bursts per unit comoving volume and the relative fraction of bursts with a certain luminosity. The construction of these two distributions, however, requires measuring the redshift. Only some GRBs EE had well redshift measurements a few years ago, such as GRB 060 614 (Gehrels et al. 2006). The LF and FR must be urgently studied with the number of GRBs EE with known redshifts increasing.

The previous studies on GRB LF and FR usually used the log N–log P distribution (Fenimore & Ramirez-Ruiz 2000; Cao et al. 2011; Sun, Zhang & Li 2015). However, the distribution is produced by the luminosity and redshift convolved (Yonetoku et al. 2004). Coward (2007) pointed out that several selection effects for the observed redshift distribution of GRBs, such as Malmquist bias, observational limit of the satellite, which is the most important selection effect. The *Swift* have a flux limit 2×10^{-8} erg cm^{-2} s^{-1}. This means that we cannot observe a GRB below the flux limit. To correct this selection effect and obtain the intrinsic LF and FR, Lynden-Bell (1971) put forward a non-parametric approach named as Lynden-Bell's c^- method to calculate the FR. This method has been applied to many transient phenomena, such as GRB (Yonetoku et al. 2004; Yu et al. 2015; Deng et al. 2016; Zhang & Wang 2018; Liu, Zhang & Zhu 2021; Dong et al. 2022, 2023), active galactic nucleus (Singal et al. 2011; Zeng, Petrosian & Yi 2021), and fast radio burst (FRB; Deng, Wei & Wu 2019). The premise of this method is that the luminosity and redshift are independent of each other. Therefore, we should first test for independence between them by using Kendall τ test method (Efron & Petrosian 1992). Importantly, Dong et al. (2023) also used the non-parameters method to investigate the progenitors of low- and high-luminosity GRB samples.

In this paper, Our main purpose is to study the LF and FR of the subclass of GRB EE using Lynden-Bell's c^- method to distinguish their origin. Section 2 introduces the sample source and K-correction method. In Sections 3 and 4, we describe the Amati relation and Lynden-Bell's c^- and Kendall τ test method in detail, respectively. In Section 5, we present the result of the LF and FR of GRB EE (EE-I and EE-II). Finally, Section 6 presents the conclusion.

2 DATA AND *K*-CORRECTION

Swift is a GRB detector with a large wide field of view that was launched at 17:16 GMT on 2004 November 20.[1] Since 2005, *Swift* has discovered approximately 1600 GRBs, of which 419 GRBs have spectral parameters (estimated redshift, fluence, and peak photon flux). This instrument also provided the light curves in different energy bands, including Channel 1 (15–25 keV), Channel 2 (25–50 keV), Channel 3 (50–100 keV), Channel 4 (100–350 keV), and Channel 5 (15–350 keV). We combined the signal-to-noise ratio (S/N $> 2\sigma$; Kaneko et al. 2015; Zhang et al. 2020a; Li et al. 2023) and Bayesian block method (Norris, Gehrels & Scargle 2010; Scargle et al. 2013; Burgess 2014; von Kienlin et al. 2019) to identify EE components from the light curves of prompt emission. Ultimately, we reserve 80 *Swift* GRBs (60 lGRBs and 20 sGRBs) with well-estimated parameters and EE components. Fig. 1 exhibits two typical examples of GRBs with EE components: GRB 080 413 and GRB 140430A. In Table 1, we list the information of GRB EE including GRB name (column 1), duration T_{90} (column 2), redshift z (column 3), low- and high-energy photon index α and β (columns 4 and 5), peak energy $E_{\rm p}$ in observer frame (column 6), peak flux P (column 7), fluence S_γ (column 8), the energy range $E_{\rm min}$–$E_{\rm max}$ (column 9), bolometric peak luminosity $L_{\rm p}$ and isotropic energy $E_{\rm iso}$ (columns 10 and 11), and the type of GRB EE (column 12).

The spectra of GRB are generally fitted by two spectral models, including Band model (Band et al. 1993) and a single/cut-off power-law model (Sakamoto et al. 2008). The form of the Band function is as follows:

$$\Phi(E) = \begin{cases} A\left(\frac{E}{100\,\rm keV}\right)^{\alpha} \exp\left(-\frac{(2+\alpha)E}{E_{\rm p}}\right), E \leq \frac{(\alpha-\beta)E_{\rm p}}{(2+\alpha)} \\ A\left(\frac{E}{100\,\rm keV}\right)^{\beta} \left(\frac{(\alpha-\beta)E_{\rm p}}{(2+\alpha)100\,\rm keV}\right) \exp(\beta-\alpha), E \geq \frac{(\alpha-\beta)E_{\rm p}}{(2+\alpha)} \end{cases}, \tag{1}$$

and the cut-off power law can be expressed as

$$\Phi(E) = B\left(\frac{E}{50\,\rm keV}\right)^{\alpha} \exp\left(-\frac{(2+\alpha)E}{E_{\rm p}}\right). \tag{2}$$

Since the peak flux is observed in different energy ranges, we will use the same K-correction method to convert the flux into the 1–10^4 keV band to get bolometric luminosities (e.g. Yu et al. 2015; Zhang et al. 2018). The bolometric luminosity can be calculated by $L = 4\pi D_{\rm L}^2(z) P_{\rm bolo}$ or $L = 4\pi D_{\rm L}^2(z) P K$. K and P are the K-correction factor and the peak flux observed in the energy range, respectively. if P is in units of erg cm^{-2} s^{-1}, the K can be

[1] https://swift.gsfc.nasa.gov/

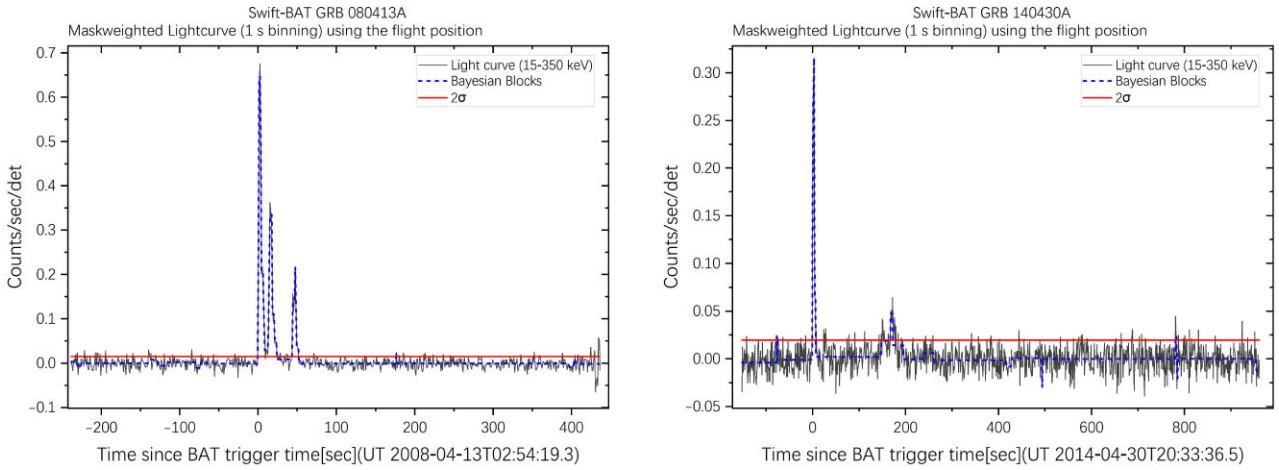

Figure 1. The light curve of prompt emission of GRB 080413A and GRB 140430A in 15–350 keV energy band. The blue dotted line shows the fitted line of the Bayesian block. The red line represents the 2σ line.

expressed as

$$K = \frac{\int_{1/(1+z)}^{10\,000/(1+z)} E\Phi(E)\,\mathrm{d}E}{\int_{E_{\min}}^{E_{\max}} E\Phi(E)\,\mathrm{d}E}, \tag{3}$$

else if P is in unit of photon cm^{-2} s^{-1}, the $P_{\rm bolo}$ can be expressed as

$$P_{\rm bolo} = P\frac{\int_{1/(1+z)}^{10\,000/(1+z)} E\Phi(E)\,\mathrm{d}E}{\int_{E_{\min}}^{E_{\max}} \Phi(E)\,\mathrm{d}E}. \tag{4}$$

The value of the flux limit is $F_{\rm lim} = 2.0 \times 10^{-8}$ erg cm^{-2} s^{-1} (Yu et al. 2015). Then, luminosity limit is given as $L_{\rm lim} = 4\pi D_{\rm L}^2(z)F_{\rm lim}$.

3 AMATI RELATION

The duration of a GRB is a key indicator of its physical origin, with lGRBs perhaps associated with the collapse of massive stars and sGRBs with mergers of neutron stars. However, there is a substantial overlap in the properties of both lGRB and sGRB. To date, no other parameter fully distinguishes the origins of these two groups, such as Li et al. (2023) who verified that both GRBs associated with supernova/kilonova comply with the Amati relations that match those of lGRBs/sGRBs, but two kinds of GRB also have obviously overlapped. Classifying GRBs based on their prompt emission is a useful task, as it has the potential to quickly identify the possible properties of their progenitor and plan the most comprehensive follow-up actions within a few minutes of detecting GRB. However, the situation in this field is puzzling due to the complexity of the GRB light curves and the diversity of possible progenitors (the combination of different types of compact stars, collapsar with or without short-lived active neutron stars, etc.). Fortunately, the sample size of GRB is large enough to establish correlation relationships for classification. The $E_{\rm p,\,i}$–$E_{\rm iso}$ relation proposed by Amati et al. (2002) is a universal method to classify the GRB into lGRB and sGRB. Amati (2006) implied the sGRB is an outlier of this correlation, so sGRB could have its own Amati relation. He found that the slope of lGRBs is 0.5 (see also Zhang et al. 2009), showing that it can be a powerful tool for discriminating different classes of GRBs and understanding their nature and differences. Zhang et al. (2018) established the $E_{\rm p,\,i}$–$E_{\rm iso}$ relationship for lGRB and sGRB, where the lGRB and sGRB distributions are in different locations, although the slopes are consistent. This claim has been challenged by some authors (Band & Preece 2005; Krimm et al. 2009; Heussaff, Atteia & Zolnierowski 2013), suggesting that the relationship is the result of selection and instrumental effects, but some authors have argued that these effects are relatively small (Amati & Della Valle 2013; Demianski et al. 2017a,b). Zhang et al. (2020a) found that reclassifying the GRB with EE into EE-I and EE-II types can result in a tighter correlation. This classification is similar to that of Qin & Chen (2013), who proposed that the GRB in the Amati plane could be divided into two groups: Amati GRB and no-Amati GRB based on the logarithmic deviation of the $E_{\rm p}$. Therefore, according to their empirical relationship, we divide our samples into two categories (see Fig. 2, right panel): Amati GRB (renamed as type EE-I) and no-Amati GRB (renamed as type EE-II), defined as GRBs that are located below and above the empirical relationship ($E_{\rm p,r,pre} = 493E_{\rm iso}^{0.57}$), and the $E_{\rm iso}$ is in units of 10^{52} erg.

The isotropic bolometric energy can be expressed as $E = 4\pi D_{\rm L}^2(z)S_\gamma K/(1+z)$, and the peak energy in the rest frame can be calculated by $E_{\rm p,\,i} = E_{\rm p}(1+z)$. Fig. 2 (left panel) shows the $E_{\rm p,\,i}$–$E_{\rm iso}$ locations of lGRB and sGRB with EE. The best fits the Amati relations of short and long bursts are taken from Zhang et al. (2018). We redivide these EE GRB into type EE-I and EE-II as Fig. 2 (right panel), according to the empirical relationship proposed by Qin & Chen (2013). Out of 56 EE-I types, 54 belong to lGRB (94 per cent), and out of 24 EE-II types, 18 belong to sGRB (75 per cent), which indicates that most EE-I-type bursts are lGRB and most non-EE-II-type bursts are of sGRBs.

4 LYNDEN-BELL'S c^- METHOD AND NON-PARAMETRIC TEST METHOD

The Lynden-Bell c^- method is an effective non-parametric method to analyse the distribution of the bolometric luminosity/energy and redshift of the astronomical objects with the truncated data sample (e.g. Yonetoku et al. 2004; Yu et al. 2015; Deng et al. 2016; Liu, Zhang & Zhu 2021; Dong et al. 2022), active galactic nucleus (Singal et al. 2011; Zeng, Petrosian & Yi 2021), and FRB (Deng, Wei & Wu 2019). This work also uses this method to study LF and FR.

If the parameters L and z are independent, the distribution of LF and redshift can be written as $\Psi(L, z) = \psi_z(L)\varphi(z)$. The $\psi_z(L)$ is LF at redshift z. A function $g(z) = (1+z)^k$ can remove the effect

Table 1. Spectral parameters of GRBs with EE.[a]

GRB	T_{90} (s)	z	α	β	$E_{\rm p}$ (keV)	P (photon cm^{-2} s^{-1})	S_γ ($\times10^{-7}$ erg cm^{-2} s^{-1})	$E_{\rm min}$–$E_{\rm max}$ (keV)	$L_{\rm p}$ ($\times10^{51}$ erg s^{-1})	$E_{\rm iso}$ ($\times10^{52}$ erg)	Type
(1)	(2)	(3)	(4)	(5)	(6)	(7)	(8)	(9)	(10)	(11)	(12)
050803	87.9	0.422	− 1.356	–	952.765	0.96 ± 0.11	21.50 ± 1.35	15–150	0.26 ± 0.03	0.51 ± 0.03	EE-II
050813	0.6	0.722	− 1.19	–	64.615	1.22 ± 0.26	1.24 ± 0.46	15–350	0.28 ± 0.06	0.02 ± 0.01	EE-II
050915A	52	2.5273	− 1.002	–	137.16	0.77 ± 0.14	8.50 ± 0.88	15–150	5.56 ± 1.01	2.19 ± 0.23	EE-I
051109A	37.2	2.346	− 1.25	–	161	3.94 ± 0.69	22.00 ± 2.72	20–500	27.76 ± 4.86	3.65 ± 0.45	EE-I
051111	47	1.55	− 1.137	–	258.32	2.66 ± 0.21	40.80 ± 1.34	15–150	8.68 ± 0.69	6.37 ± 0.21	EE-I
051221A	1.4	0.547	− 1.08	–	402	4.70 ± 0.80	24.00 ± 4.00	20–2000	1.42 ± 0.24	0.20 ± 0.03	EE-II
060418	103.1	1.49	− 1.553	–	182.814	6.52 ± 0.35	83.30 ± 2.53	15–150	15.53 ± 0.83	11.34 ± 0.34	EE-I
060502B	0.131	0.287	− 0.11	–	117.949	0.62 ± 0.12	0.40 ± 0.05	15–150	0.02 ± 0.00	0.00 ± 0.00	EE-II
060526	298.2	3.21	− 0.336	–	89.792	1.67 ± 0.18	12.60 ± 1.65	15–150	16.02 ± 1.73	3.55 ± 0.46	EE-I
060607A	102.2	3.082	− 1.147	–	149.843	1.40 ± 0.13	25.50 ± 1.12	15–150	17.22 ± 1.60	9.92 ± 0.44	EE-I
060614[d]	108.7	0.13	− 2.037	–	98.52	11.50 ± 0.74	204.00 ± 3.63	15–150	0.24 ± 0.02	0.61 ± 0.01	EE-I
060708	10.2	1.92[b]	− 1.22	–	88.948	1.94 ± 0.14	4.94 ± 0.37	15–150	5.90 ± 0.43	0.73 ± 0.05	EE-I
060719	66.9	1.532	− 1.63	–	68.556	2.16 ± 0.20	15.00 ± 0.91	15–150	4.35 ± 0.40	1.86 ± 0.11	EE-I
060814	145.3	1.9229[b]	− 1.412	–	302.336	7.27 ± 0.29	146.00 ± 2.39	15–150	40.41 ± 0.61	36.85 ± 0.60	EE-I
060904B[c]	171.5	0.703	− 1.234	–	84.094	2.44 ± 0.21	16.20 ± 1.43	15–150	0.61 ± 0.05	0.34 ± 0.03	EE-I
060927	22.5	5.6	− 0.7	–	70.673	2.70 ± 0.17	11.30 ± 0.68	15–150	85.99 ± 5.41	7.68 ± 0.46	EE-I
061007	75.3	1.261	− 0.7	−2.61	498	14.60 ± 0.37	444.00 ± 5.62	20–10 000	37.11 ± 0.94	18.66 ± 0.24	EE-I
061110A	40.7	0.758	− 1.556	–	240.328	0.53 ± 0.12	10.60 ± 0.76	15–150	0.26 ± 0.06	0.42 ± 0.03	EE-II
061201[d]	0.21	0.111	− 0.36	–	873	3.50 ± 0.35	53.30 ± 7.00	20–3000	0.07 ± 0.01	0.02 ± 0.00	EE-II
070103	18.6	2.6208	− 1.223	–	46.633	1.04 ± 0.15	3.38 ± 0.46	15–150	5.62 ± 0.81	0.83 ± 0.11	EE-I
070208	47.7	1.165	− 1.651	–	51.29	0.90 ± 0.22	4.45 ± 1.01	15–150	0.88 ± 0.22	0.33 ± 0.07	EE-I
070429B	0.47	0.904	− 1.099	–	72.852	1.76 ± 0.24	0.63 ± 0.10	15–150	0.74 ± 0.10	0.02 ± 0.00	EE-II
070612A	368.8	0.617	− 1.439	–	137.695	1.51 ± 0.38	106.00 ± 6.01	15–150	0.35 ± 0.09	2.16 ± 0.12	EE-I
070721B	340	3.626	− 0.41	–	224.25	1.50 ± 0.30	36.00 ± 2.00	15–150	45.63 ± 9.13	23.62 ± 1.31	EE-I
070724A	0.4	0.457	− 1.15	–	82	0.94 ± 0.09	0.30 ± 0.03	15–150	0.08 ± 0.01	0.00 ± 0.00	EE-II
071227	1.8	0.383	− 0.7	–	1000	1.68 ± 0.17	16.00 ± 2.00	20–13 000	0.50 ± 0.05	0.06 ± 0.01	EE-II
080310	365	2.4266	− 1.65	–	23.284	1.30 ± 0.20	23.00 ± 2.00	15–150	7.71 ± 1.19	7.39 ± 0.64	EE-I
080413A	46	2.433	− 1.2	–	170	5.60 ± 0.20	35.00 ± 1.00	15–1000	36.51 ± 1.30	5.44 ± 0.16	EE-I
080413B	8	1.1	− 1.26	–	73.3	18.70 ± 0.80	32.00 ± 1.00	15–150	13.54 ± 0.58	1.63 ± 0.05	EE-I
080430	16.2	0.767	− 1.645	–	151.587	2.60 ± 0.20	12.00 ± 1.00	15–150	1.15 ± 0.09	0.44 ± 0.04	EE-I
080603B	60	2.69	− 1.21	–	71	3.50 ± 0.20	24.00 ± 1.00	15–150	22.24 ± 1.27	6.13 ± 0.26	EE-I
080607	79	3.036	− 0.76	−2.57	348	23.10 ± 1.10	240.00 ± 0.00	20–4000	380.20 ± 18.10	49.45 ± 0.00	EE-I
080707	27.1	1.23	− 1.397	–	29.067	1.00 ± 0.10	5.20 ± 0.60	15–150	0.90 ± 0.09	0.39 ± 0.04	EE-I
080810	106	3.35	− 2.5	−1.2	2523	2.00 ± 0.20	46.00 ± 2.00	15–1000	115.94 ± 6.13	19.50 ± 0.08	EE-II
080905A	1	0.1218	0.12	−2.35	311.2	6.32 ± 0.20	8.51 ± 0.20	10–1000	0.05 ± 0.00	0.00 ± 0.00	EE-II
080905B	128	2.374	− 1.579	–	256.097	0.50 ± 0.10	18.00 ± 2.00	15–150	4.27 ± 0.85	6.43 ± 0.71	EE-I
090205	8.8	4.7	− 0.394	–	38.42	0.50 ± 0.10	1.90 ± 0.30	15–150	8.11 ± 1.62	19.50 ± 0.15	EE-I
090407	310	1.4485	− 1.585	–	309.959	0.60 ± 0.10	11.00 ± 2.00	15–150	1.63 ± 0.27	1.71 ± 0.31	EE-II
090424	48	0.544	− 1.19	–	108.6	71.00 ± 2.00	210.00 ± 0.00	15–150	10.47 ± 0.29	2.74 ± 0.00	EE-I
090426A	1.2	2.609	− 1.105	–	55.08	2.40 ± 0.30	1.80 ± 0.30	15–150	12.61 ± 1.58	0.41 ± 0.07	EE-I
090510	0.3	0.903	− 0.86	−2.58	4302	40.95 ± 4.10	33.70 ± 3.40	10–1000	210.78 ± 21.10	0.72 ± 0.07	EE-II
090530	48	1.266	− 1.078	–	92.142	2.50 ± 0.30	11.00 ± 1.00	15–150	2.66 ± 0.32	0.71 ± 0.06	EE-I
090618[c]	113.2	0.54	− 1.42	–	134	38.90 ± 0.80	1050.00 ± 10.00	15–150	6.49 ± 0.13	15.94 ± 0.15	EE-I
090715B	266	3	− 1.1	–	134	3.80 ± 0.20	57.00 ± 2.00	20–2000	43.63 ± 2.30	13.10 ± 0.46	EE-I
100425A	37	1.755	− 0.885	–	25.353	1.40 ± 0.20	4.70 ± 0.90	15–150	2.44 ± 0.35	0.62 ± 0.12	EE-I
100704A	197.5	3.6	− 0.76	−2.53	178.3	4.30 ± 0.20	60.00 ± 2.00	10–1000	53.66 ± 2.50	16.30 ± 0.54	EE-I
100724	1.4	1.288	− 0.51	–	42.5	1.56 ± 0.16	1.41 ± 0.14	15–150	1.15 ± 0.12	0.08 ± 0.01	EE-I
100728A	198.5	1.567	− 0.76	–	357.7	5.10 ± 0.20	380.00 ± 0.00	50–300	37.53 ± 1.47	51.73 ± 0.00	EE-I
100906A	114.4	1.727	− 1.34	−1.98	106	10.10 ± 0.40	120.00 ± 0.00	50–300	78.21 ± 205.15	28.71 ± 0.91	EE-I
110715A	13	0.82	− 1.23	−2.7	120	53.90 ± 1.10	118.00 ± 2.00	20–10 000	22.23 ± 125.09	2.73 ± 10.40	EE-I
111008A	63.46	5	− 1.36	–	149	6.40 ± 0.70	53.00 ± 3.00	20–2000	275.27 ± 30.11	29.35 ± 1.66	EE-I
111228A[c]	101.2	0.71627	− 1.9	–	34	12.40 ± 0.50	85.00 ± 2.00	50–300	17.92 ± 0.72	4.43 ± 0.10	EE-I
120729A[c]	71.5	0.8	− 0.78	–	64.985	2.90 ± 0.20	24.00 ± 1.00	15–150	0.80 ± 0.06	0.54 ± 0.02	EE-I
121027A	62.6	1.773	− 1.58	–	82.46	1.30 ± 0.20	20.00 ± 1.00	15–150	3.77 ± 0.58	3.19 ± 0.16	EE-I
130427A[c]	162.83	0.3399	− 0.789	−3.06	830	331.00 ± 4.60	3100.00 ± 30.00	10–1000	46.60 ± 0.65	8.98 ± 0.09	EE-I
130514A	204	3.6	− 1.44	−2.5	108	2.80 ± 0.30	91.00 ± 2.00	15–1200	36.62 ± 3.92	33.52 ± 0.74	EE-I
130603B[d]	0.18	0.356	− 0.73	–	660	1.30 ± 0.20	66.00 ± 7.00	20–15 000	0.23 ± 0.04	0.21 ± 0.02	EE-II
130907A	>360	1.238	− 0.91	−2.42	394	25.60 ± 0.50	1400.00 ± 10.00	20–10 000	47.45 ± 0.93	58.55 ± 0.42	EE-I
131004	1.54	0.71	− 1.36	−22.09	118.1	9.82 ± 0.98	5.09 ± 0.51	10–1000	2.09 ± 0.21	0.08 ± 0.01	EE-II
140430A	173.6	1.6	− 2.108	–	47.62	2.50 ± 0.20	11.00 ± 2.00	15–150	514.51 ± 41.16	141.31 ± 25.69	EE-I
140506A	111.1	0.889	− 0.9	−2	141	10.90 ± 0.90	28.00 ± 3.00	50–300	12.41 ± 1.02	0.95 ± 0.10	EE-I
140903A[d]	0.3	0.351	− 1.36	–	44.169	2.50 ± 0.20	1.40 ± 0.10	15–150	0.10 ± 0.01	0.01 ± 0.00	EE-II
141004A[c]	3.92	0.57	− 1.3	–	147	6.10 ± 0.30	6.70 ± 0.30	50–300	2.85 ± 0.14	0.11 ± 0.01	EE-II
141212A	0.3	0.569	− 1.146	–	94.865	1.20 ± 0.20	0.72 ± 0.12	15–150	0.18 ± 0.03	0.01 ± 0.00	EE-II

Table 1 – *continued*

GRB	T_{90} (s)	z	α	β	E_p (keV)	P (photon cm^{-2} s^{-1})	S_γ ($\times10^{-7}$ erg cm^{-2} s^{-1})	E_{min}–E_{max} (keV)	L_p ($\times10^{51}$ erg s^{-1})	E_{iso} ($\times10^{52}$ erg)	Type
(1)	(2)	(3)	(4)	(5)	(6)	(7)	(8)	(9)	(10)	(11)	(12)
150120A	1.2	0.46	−1.43	−1.65	130	3.10 ± 0.30	3.40 ± 0.80	10–1000	0.42 ± 0.02	0.04 ± 0.01	EE-II
150423A	0.22	1.394	0.43	–	120	0.90 ± 0.10	0.63 ± 0.10	15–150	1.55 ± 0.17	0.04 ± 0.01	EE-II
151027A	129.69	0.81	−1.41	–	340	6.80 ± 0.60	78.00 ± 2.00	50–300	10.36 ± 0.91	3.47 ± 0.09	EE-I
160227A	316.5	2.38	−0.75	–	65.8	0.60 ± 0.10	31.00 ± 2.00	15–150	2.42 ± 0.40	5.38 ± 0.35	EE-I
160410A	8.2	1.717	−0.71	–	1416	3.50 ± 0.30	7.80 ± 0.80	20–10 000	51.14 ± 4.38	0.54 ± 0.06	EE-II
160425A	304.58	0.555	−1.975	–	5.251	2.80 ± 0.20	21.00 ± 2.00	15–150	0.56 ± 0.04	0.48 ± 0.05	EE-I
160624A	0.2	0.483	−0.63	−3.65	1168	6.39 ± 0.64	1.21 ± 0.12	10–1000	3.35 ± 0.41	0.01 ± 0.00	EE-II
160824B	0.48	0.16	−0.12	5.38	46.32	1.68 ± 0.17	1.03 ± 0.10	15–150	0.01 ± 0.00	0.00 ± 0.00	EE-II
161017A	216.3	2.0127	−1.04	–	298.5	2.80 ± 0.20	53.00 ± 2.00	50–300	34.32 ± 2.45	10.89 ± 0.41	EE-I
161108A	105.1	1.159	−1.312	–	65.124	0.60 ± 0.10	11.00 ± 1.00	15–150	0.49 ± 0.08	0.63 ± 0.06	EE-I
170705A	217.3	2.01	−0.88	−2.38	100	13.90 ± 0.40	95.00 ± 3.00	50–300	104.92 ± 3.02	18.62 ± 0.59	EE-I
180329B	210	1.998	−0.97	–	48.6	1.40 ± 0.40	33.00 ± 3.00	15–150	3.54 ± 1.01	4.53 ± 0.41	EE-I
180620B	198.8	1.1175	−0.85	–	149	3.60 ± 0.20	100.00 ± 3.00	15–150	3.74 ± 0.21	5.88 ± 0.18	EE-I
190719C	185.7	2.469	−0.87	–	81	5.50 ± 0.30	51.00 ± 3.00	50–300	75.14 ± 4.10	13.17 ± 0.77	EE-I
200522A[d]	0.62	0.554	−0.54	–	77.76	1.50 ± 0.20	1.10 ± 0.10	15–150	0.08 ± 0.01	0.01 ± 0.00	EE-II
210619B	60.9	1.937	−1.25	–	286.165	115.00 ± 2.20	950.00 ± 10.00	15–150	666.57 ± 12.75	235.66 ± 2.48	EE-I

Notes. [a]The spectral parameters in this paper are acquired from Yu et al. (2015), Zhang & Wang (2018), Gamma-ray Coordinates Network (GCN) at https://gcn.gsfc.nasa.gov/, https://www.mpe.mpg.de/ jcg/grbgen.html, and the official *Swift* website https://swift.gsfc.nasa.gov/results/batgrbcat/
[b]The values of redshift of GRB 060708 and GRB 060814 come from Hjorth (2012).
[c]The GRB is associated with supernovae.
[d]The GRB is associated with kilonovae.

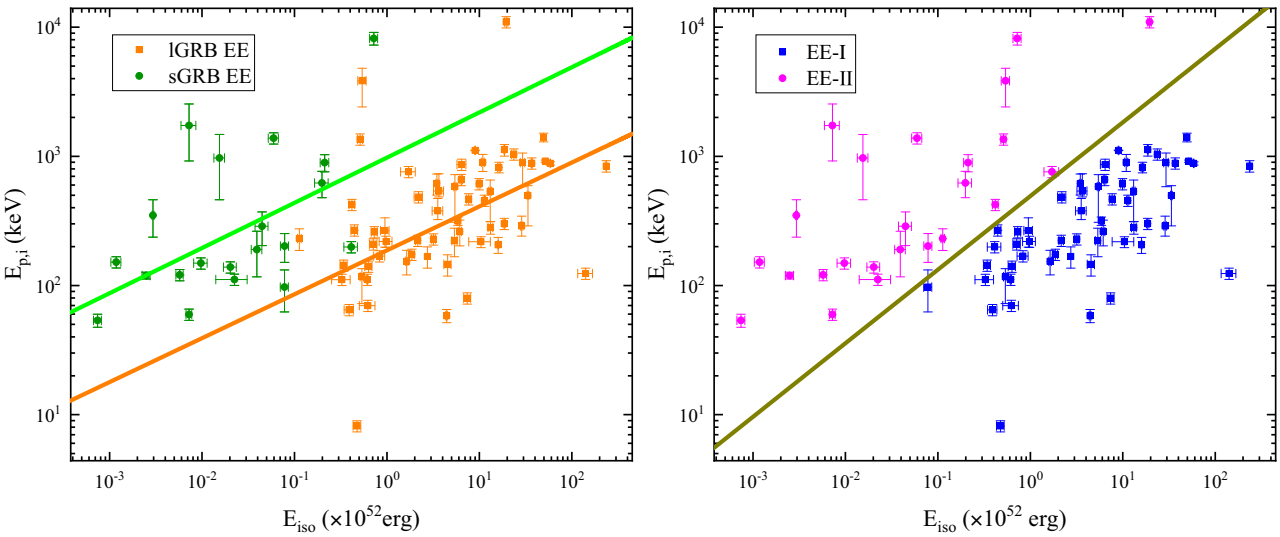

Figure 2. Left: the distribution of 60 lGRB (orange rectangles) and 20 sGRB (green dots) in the $E_{p,i}$–E_{iso} plane. The best solid orange and green fitting lines are derived from Zhang et al. (2018) for normal lGRB and sGRB. Right: the distribution of 56 EE-I (blue rectangle) and 24 EE-II GRB (purple dots) in the $E_{p,i}$–E_{iso} plane. The brown solid line is taken from Qin & Chen (2013).

of luminosity evolution. Then the L will transform into $L_0 = L/g(z)$. Therefore, $\Psi(L, z)$ can write as $\psi(L_0)\varphi(z)$.

We use the non-parametric test method raised by Efron & Petrosian (1992) to derive the evolution function $g(z)$. In the (L, z) plane as shown in Fig. 3, for the ith point (L_i, z_i), we can define J_i as

$$J_i = \{j | L_j \geq L_i, z_j \leq z_i^{\max}\}, \tag{5}$$

where L_i is the luminosity of the ith GRB EE and $z_i^{\max}$ is the maximum redshift at which a GRB EE (EE-I and EE-II) with the luminosity L_i can be detected by *Swift* detector. This range is shown as a black rectangle in Fig. 3. The number included in this range is n_i, and the N_i is defined as $n_i - 1$, which means take ith out, and the J_i^1 also can be defined as

$$J_i^1 = \{j | L_j \geq L_i^{\min}, z_j \leq z_i\}, \tag{6}$$

where $L_i^{\min}$ is the limit luminosity at the redshift z_i. This range is shown as the red rectangle in Fig. 3. The number included in this region is M_i.

In the black rectangle, R_i is defined as the events number that have redshift z less than z_i. R_i should be uniformly distributed between 1 and n_i based on the fact that L and z are independent. The Kendall τ test statistic is (Efron & Petrosian 1992)

$$\tau = \sum_i \frac{(R_i - E_i)}{\sqrt{V_i}}, \tag{7}$$

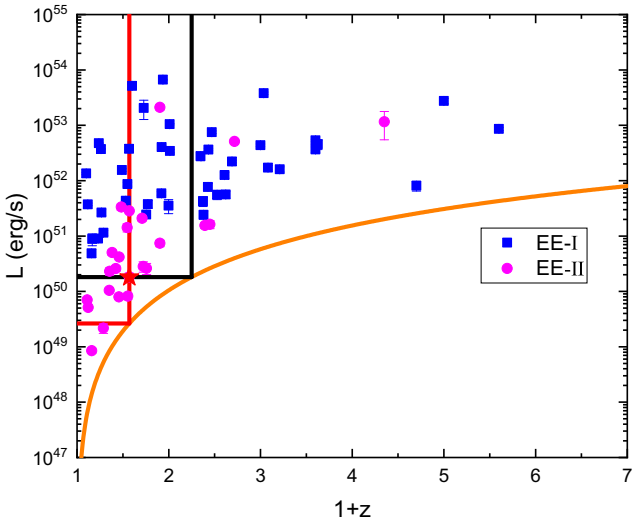

Figure 3. The distribution of luminosity and redshift in the L–z plane. The blue squares and purple dots represent the EE-I and EE-II GRBs, respectively. The flux limit is 2×10^{-8} erg cm^{-2} s^{-1}.

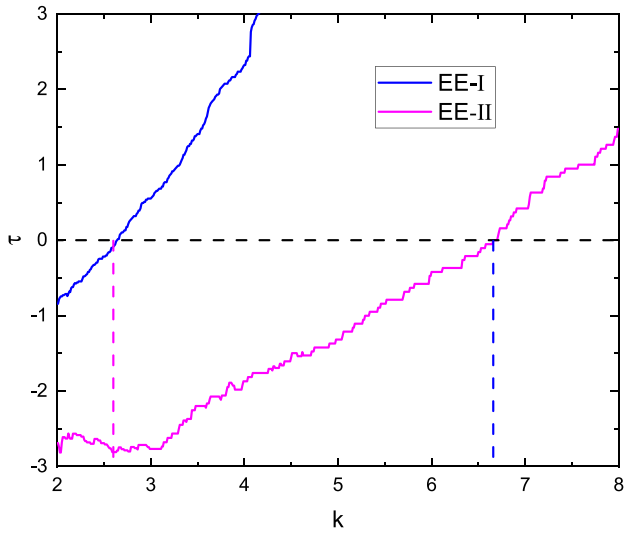

Figure 4. The evolution of τ as k. The blue and purple dotted lines represent the k value when the $\tau = 0$ for EE-I and EE-II GRBs, respectively.

where $E_i = \frac{1+n_i}{2}$ and $V_i = \frac{n_i^2-1}{12}$ are, respectively, the expected mean and variance of R_i. τ will be zero if the size of the sample of $R_i \leq E_i$ is equal to the size of the sample with $R_i \geq E_i$. After we find the function form of $g(z)$, the effection of luminosity evolution can be removed by transforming L into L_0.

L and z are independent on each other until the test statistic τ is zero by changing the value of k. We show how τ changes with varying k. The k value is 2.64 and 6.66 for EE-I and EE-II, respectively, in Fig. 4.

Therefore, the non-evolving luminosity can be written as $L_0 = L/(1+z)^k$ in Fig. 5. We can use a non-parametric method to derive the local cumulative LF distribution from the following equation (Lynden-Bell 1971; Efron & Petrosian 1992):

$$\Psi(L_{0i}) = \prod_{j<i}\left(1+\frac{1}{N_j}\right), \tag{8}$$

and the cumulative number distribution can be obtained from

$$\phi(z_i) = \prod_{j<i}\left(1+\frac{1}{M_j}\right). \tag{9}$$

Next, the FR can be calculated by

$$\rho(z) = \frac{\mathrm{d}\phi(z)}{\mathrm{d}z}(1+z)\left(\frac{\mathrm{d}V(z)}{\mathrm{d}z}\right)^{-1}, \tag{10}$$

where the $\frac{\mathrm{d}V(z)}{\mathrm{d}z}$ is the differential comoving volume, which can be expressed as

$$\frac{\mathrm{d}V(z)}{\mathrm{d}z} = 4\pi\left(\frac{c}{H_0}\right)^3\left(\int_0^z \frac{\mathrm{d}z}{\sqrt{1-\Omega_\mathrm{m}+\Omega_\mathrm{m}(1+z)^3}}\right)^2 \times\left(\frac{1}{\sqrt{1-\Omega_\mathrm{m}+\Omega_\mathrm{m}(1+z)^3}}\right), \tag{11}$$

and the expected number of GRBs can be estimated by (Lan et al. 2019)

$$N_\mathrm{exp} = \frac{\Delta\Omega T}{4\pi}\int_0^{z_\mathrm{max}}\frac{\rho(z)}{1+z}\frac{\mathrm{d}V(z)}{\mathrm{d}z}\mathrm{d}z\int_{\max[L_\mathrm{min},L_\mathrm{lim}(z)]}^{L_\mathrm{max}}\psi(L)\,\mathrm{d}L. \tag{12}$$

The *Swift* instrument has been running for approximately $T = 19$ yr. The field of view of this telescope is $\Omega = 1.33$ sr (Sun, Zhang & Li 2015).

5 RESULT

In this section, we present the LF and FR of subclasses of GRBs EE, respectively.

5.1 Luminosity function

Fig. 6 shows the distribution of normalized luminosity function (LF) $\psi(L_0)$. Using the broken power law, we can fit this curve to obtain the forms of LF for the dim segment and bright segment for EE-I GRB as

$$\psi(L_0) \propto \begin{cases} L_0^{-0.34\pm0.01}, L_0 < L_0^\mathrm{b} \\ L_0^{-0.67\pm0.02}, L_0 > L_0^\mathrm{b} \end{cases}, \tag{13}$$

and for EE-II as

$$\psi(L_0) \propto \begin{cases} L_0^{-0.43\pm0.02}, L_0 < L_0^\mathrm{b} \\ L_0^{-0.93\pm0.01}, L_0 > L_0^\mathrm{b} \end{cases}, \tag{14}$$

where break point $L_0^\mathrm{b} = 3.03 \times 10^{49}$ erg s^{-1} for EE-II GRBs, which is small two order than the break luminosity $L_0^\mathrm{b} = 1.00 \times 10^{51}$ erg s^{-1} of EE-I GRBs. Yu et al. (2015) described the cumulatively luminosity distribution by a broken power-law function with $\alpha = -0.14 \pm 0.02$, $\beta = -0.7 \pm 0.03$, $L_0^\mathrm{b} = 1.43 \times 10^{51}$ erg s^{-1} for 127 lGRBs. Pescalli et al. (2016) estimated the luminosity distribution of complete 99 lGRBs with $\alpha = -1.32 \pm 0.21$, $\beta = -1.84 \pm 0.24$, $L_0^\mathrm{b} = 2.82 \times 10^{51}$ erg s^{-1}. Wanderman & Piran (2015) used sGRB, which originated from non-core collapsars to estimate the LF and FR, and they acquire the breaking point as $L^\mathrm{b} = 2.0 \times 10^{52}$ erg s^{-1} with power-law indices of 0.95 and 2.0 for the dim and bright segments, respectively. Liu, Zhang & Zhu (2021) used 324 *Fermi* sGRB to derive the break point as $\alpha = -0.45 \pm 0.01$, $\beta = -1.11 \pm 0.01$, with the break luminosity $L_0^\mathrm{b} = 4.92 \times 10^{49}$ erg s^{-1}. It is worth noting that this result is roughly consistent with our work. The break luminosity of EE-I GRBs is larger by two orders than EE-II GRBs, similar to lGRB to sGRB after

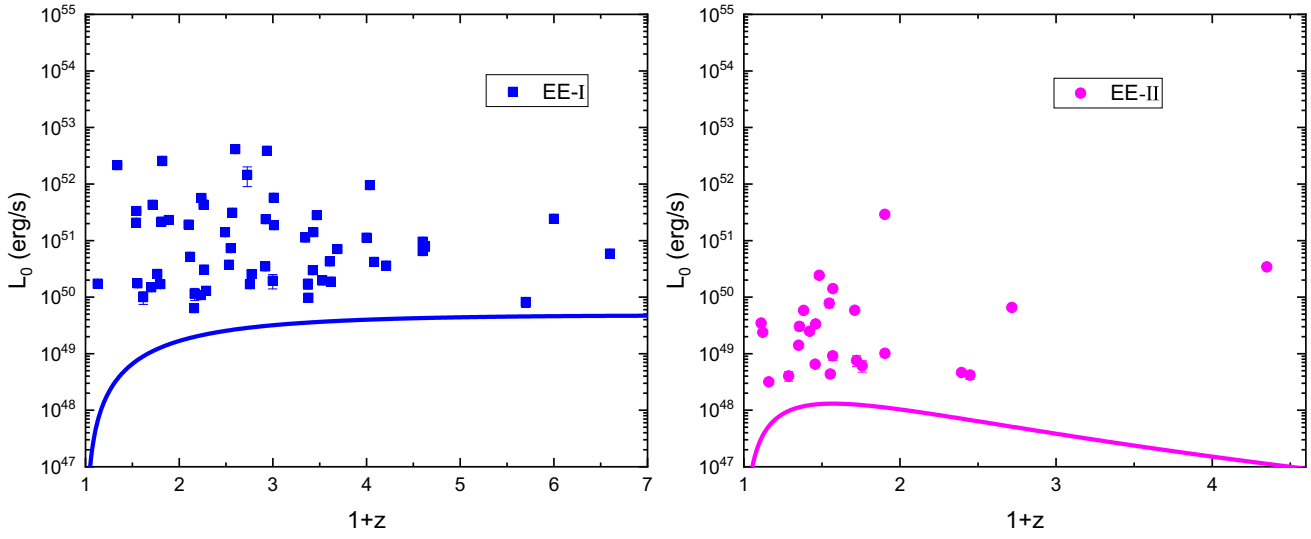

Figure 5. Non-evolving luminosity $L_0 = L/(1+z)^k$ of 60 GRBs EE (56 EE-I GRBs and 24 EE-II GRBs) above the truncation line. The k value is 2.64 and 6.66 for EE-I GRB and EE-II GRB, respectively.

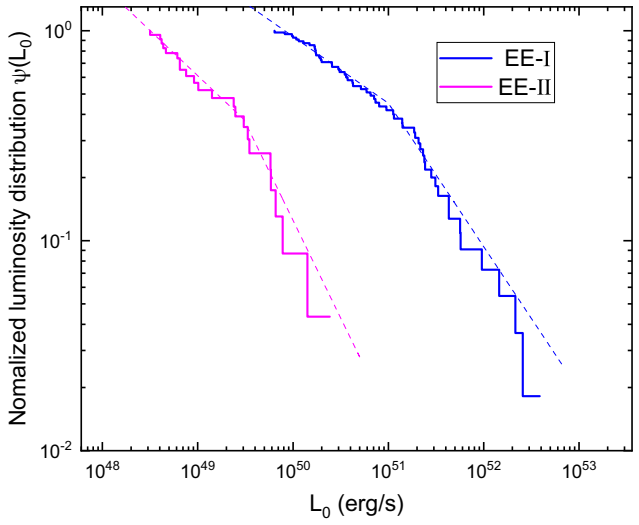

Figure 6. The distribution of local luminosity function (LF) for 56 EE-I GRBs and 24 EE-II GRBs. This fitted form can be expressed as $\psi(L_0) \propto L_0^{-0.34\pm0.01}$ for the dim segment and $\psi(L_0) \propto L_0^{-0.67\pm0.02}$ for the bright segment with EE-I GRB, the broken point is $L_0^{\rm b} = 1.00 \times 10^{51}\,{\rm erg\,s^{-1}}$. For EE-II GRBs, the form can be expressed as $\psi(L_0) \propto L_0^{-0.42\pm0.02}$ for the dim segment and $\psi(L_0) \propto L_0^{-0.93\pm0.01}$ for the bright segment, the broken point is $L_0^{\rm b} = 3.03 \times 10^{49}\,{\rm erg\,s^{-1}}$.

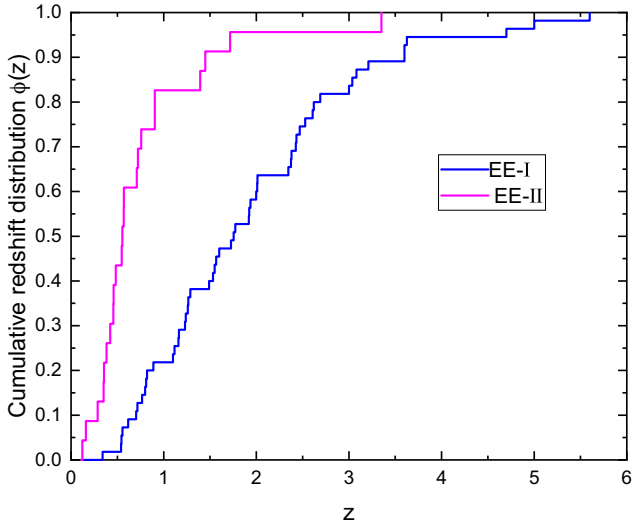

Figure 7. The normalized cumulative distribution of redshift for 56 EE-I and 24 EE-II GRBs.

removing the luminosity evolution with redshift. We must emphasize that the LF only presents the local distribution at $z = 0$. Therefore, the LF at redshift z will be rewritten as $\psi_z(L) = \psi(L/g(z)) = \psi(L/(1+z)^k)$. The break point is $L_z^{\rm b} = L_0^{\rm b}(1+z)^k$ at z.

5.2 Formation rate

Fig. 7 shows the normalized cumulative distribution of redshift $\phi(z)$. From equation (10), we can calculate the formation rate (FR) of GRB EE. First, the differential cumulative redshift distribution form should be derived. In Fig. 8, the blue and purple stepwise line is the FR of GRBs EE. It is obvious that EE-II GRBs have kept a decreasing trend. The error bars are calculated by the GRBs number of black or red rectangle, M_j and N_j. The final error of the FR is obtained through the error transfer formula. The error bar gives a 1σ Poisson error (Gehrels 1986). We also fit the different segments using the broken power-law function. The forms of FR for EE-I GRB can be expressed as

$$\rho(z) = \rho_{\rm GRB}(0) \begin{cases} (1+z)^{-0.34\pm0.04}, z < z_0 \\ (1+z)^{-2.34\pm0.24}, z > z_0 \end{cases}, \quad (15)$$

and for EE-II GRB as

$$\rho(z) = \rho_{\rm GRB}(0) \begin{cases} (1+z)^{-1.05\pm0.03}, z < z_0 \\ (1+z)^{-8.44\pm1.10}, z > z_0 \end{cases}, \quad (16)$$

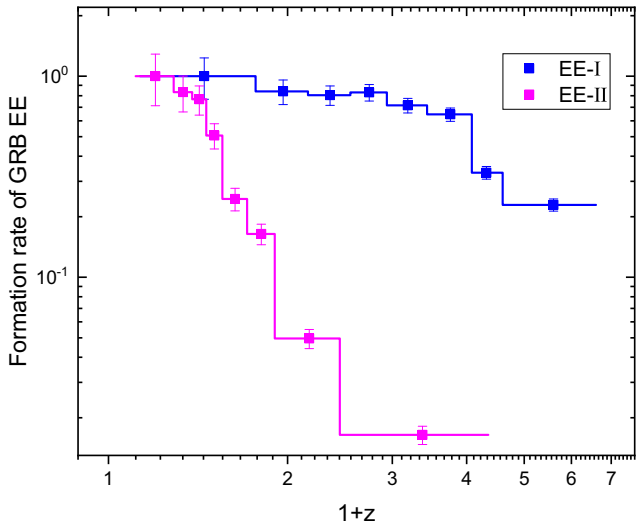

Figure 8. The formation rate (FR) for 56 EE-I and 24 EE-II GRBs. The fit function can be write as $\rho(z) \propto (1+z)^{-0.34\pm0.04}$ for $z < 2.39$ and $\rho(z) \propto (1+z)^{-2.34\pm0.24}$ for $z > 2.39$ for EE-I GRBs. The FR of EE-II can describe as $\rho(z) \propto (1+z)^{-1.05\pm0.03}$ for $z < 0.43$ and $\rho(z) \propto (1+z)^{-8.44\pm1.10}$ for $z > 0.43$.

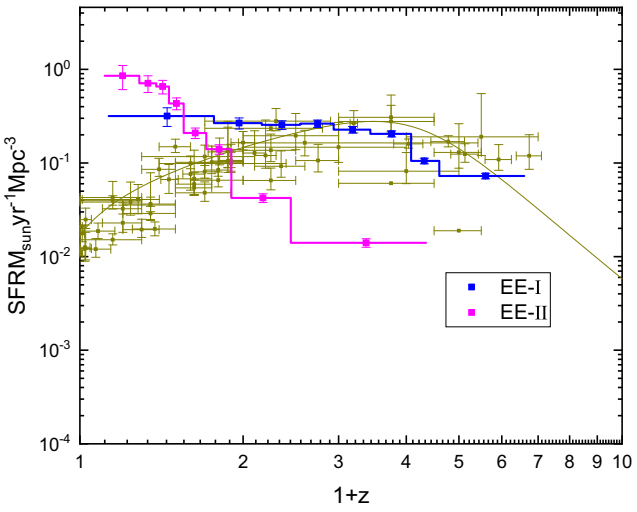

Figure 9. The FR for 56 EE-I and 24 EE-II GRBs. The data of SFR are taken from Hopkins & Beacom (2006).

where break point is $z_0 = 2.39$ for EE-I GRB and $z_0 = 0.43$ for EE-II GRB, the local FR is $\rho(0) = 0.03\,\mathrm{Gpc^{-3}\,yr^{-1}}$ for EE-I GRBs and $\rho(0) = 0.32\,\mathrm{Gpc^{-3}\,yr^{-1}}$ for EE-II GRBs according equation (12). Yu et al. (2015) found that the power-law index of FR of 127 *Swift* lGRB is 0.04 ± 0.94 for $z < 1$, -0.94 ± 0.11 for $1 < z < 4$, and -4.36 ± 0.48 for $z > 4$, and the local FR is $\rho(0) = 7.3 \pm 2.7\,\mathrm{Gpc^{-3}\,yr^{-1}}$. Importantly, they stress that the GRB rate exceeds the SFR at $z < 1$. However, Pescalli et al. (2016) found that the GRB rate increases to $z = 2$ using the complete lGRB. They suggested that the low-redshift excess was caused by an incomplete sample, and their results showed that the rate of GRB had a similar trend with SFR. Palmerio & Daigne (2021) used models to fit the three observational parameters constrained, including intensity, spectrum, and redshift, and they noted the distribution of lGRB rate follows the shape of cosmic SFR with $a = 1.35 \pm 0.10$, $b = -0.18 \pm 0.02$, the break redshift $z_\mathrm{m} = 2.2 \pm 0.10$ if an LF does not evolve with redshift ($k_\mathrm{evol} = 0$), and $\rho(0) = 0.77 \pm 0.05\,\mathrm{Gpc^{-3}\,yr^{-1}}$. The local FR of $\rho(0) = 0.03\,\mathrm{Gpc^{-3}\,yr^{-1}}$ for EE-I GRBs appears very low, compared to the rate of lGRBs, which is of the order of $1\,\mathrm{Gpc^{-3}\,yr^{-1}}$. This could be due to the small fraction of Type I GRBs with EE.

Based on empirical relationships proposed by Yonetoku et al. (2004), Liu, Zhang & Zhu (2021) obtained the FR of *Fermi* sGRB that can be described as $a = -4.02 \pm 1.34$, $b = 4.93 \pm 0.30$, and the break redshift $z_\mathrm{m} = 0.4 \pm 0.10$. They also estimate the local sGRB FR is $\rho(0) = 17.43 \pm 0.12\,\mathrm{Gpc^{-3}\,yr^{-1}}$.

Fig. 9 shows the SFR compared with the FR of EE-I and EE-II GRBs. From the qualitative perspective, the FR of EE-I GRB is roughly consistent with SFR at $z > 1$. There is still fierce debate regarding the excess of $z < 1$. Possible reasons include completeness, unclear definition of T_{90}, different origins of high- and low-luminosity bursts, etc. (Pescalli et al. 2016; Dong et al. 2022, 2023).

Table 1 lists samples associated with supernovae and kilonovae (Li et al. 2023). The GRB associated with supernovae and kilonovae is believed to originate from the death of massive stars and the merger of binary compact objects, respectively. According to the statistical results, there are a total of six supernova GRBs and five kilonovae GRBs with EE. It is worth emphasizing that EE not only exists in Type I GRB (compact star) but also in Type II GRB (massive star; Li, Zhang & Yuan 2020), and it is not a unique process for a particular type of GRB. It is a generic process that commonly exists in these two kinds of GRBs.

6 CONCLUSION

GRBs are brief and violent gamma-ray explosions in the universe, lasting from a few milliseconds to a few thousand seconds. GRBs are essential tools for tracing star formation history and studying the merger of compact objects. Using non-parametric methods to investigate the LF and FR can better understand the intrinsic properties of GRB with EE, because the coevolution between redshift and luminosity can be removed.

In this work, we used for the first time 80 GRBs with EE (56 EE-I and 24 EE-II) that have known redshifts and well-measured spectra parameters to drive the bolometric luminosity. Then, we used a non-parametric method to derive the isotropic luminosity and FR based on the constructed L–z plane. Before that, we had addressed the flux-truncation effect by the Kendall τ method. In our analysis, the evolution function $g(z) = (1+z)^k$ can transform L into L_0. The normalized luminosity distribution can be fitted by a broken power law after removing the redshift dependence. This fitted form can be expressed as $\psi(L_0) \propto L_0^{-0.34\pm0.01}$ for the dim segment and $\psi(L_0) \propto L_0^{-0.67\pm0.02}$ for bright segment with EE-I GRB, the broken point is $L_0^\mathrm{b} = 1.00 \times 10^{51}\,\mathrm{erg\,s^{-1}}$. The form can be expressed as $\psi(L_0) \propto L_0^{-0.43\pm0.02}$ for dim segment and $\psi(L_0) \propto L_0^{-0.93\pm0.01}$ for bright segment with EE-II GRB, the broken point is $L_0^\mathrm{b} = 3.03 \times 10^{49}\,\mathrm{erg\,s^{-1}}$.

We also found that the FR of the GRB EE subclass keeps decreasing and that a broken power law can fit it. The fitting function of EE-I GRBs can be written as $\rho(z) \propto (1+z)^{-0.34\pm0.04}$ for $z < 2.39$ and $\rho(z) \propto (1+z)^{-2.34\pm0.24}$ for $z > 2.39$. The FR of EE-II can describe as $\rho(z) \propto (1+z)^{-1.05\pm0.03}$ for $z < 0.43$ and $\rho(z) \propto (1+z)^{-8.44\pm1.10}$ for $z > 0.43$. Using equation (10), the local FR is $\rho(0) = 0.03\,\mathrm{Gpc^{-3}\,yr^{-1}}$ for EE-I GRBs and $\rho(0) = 0.32\,\mathrm{Gpc^{-3}\,yr^{-1}}$ for EE-II GRBs. It can be found that the FRs of EE-I and EE-II GRBs are significantly different (see Fig. 8), which further suggests

that these two kinds of GRB may have different origins. It is worth noting that it is difficult to search for EE-II GRBs at high redshifts because they are weaker in luminosity than EE-I GRBs, and current instruments are not sensitive to EE-II GRBs above $z > 1$. This leads to a relatively small number of EE-II GRBs at high redshift. Therefore, our result is speculative to derive a reliable FR for EE-II GRBs at $z > 1$. When the sensitivity of instruments is further improved, the results would be more reliable if a sample of high-redshift E-II bursts is adopted in the future.

Since EE-I GRBs have a similar position in the Amati relation to lGRBs, which are thought to originate from core collapse, we further compare the FR of EE-I GRBs with the SFR. The results of the comparison show that the evolution of the FR of EE-I GRBs is similar to that of the SFR (see Fig. 9), suggesting that EE-I GRBs may arise from the death of massive stars, whereas EE-II GRBs, which are unrelated to the SFR, may come from other processes unrelated to the SFR. Therefore, we suggest the GRB with EE could have multiple production channels from the perspective of their FRs.

ACKNOWLEDGEMENTS

This work was supported by the Basic Research Project of Yunnan Province (grant no. 202301AT070352). The data in this paper are acquired from Yu et al. (2015), Zhang & Wang (2018), Gamma-ray Coordinates Network (GCN) at https://gcn.gsfc.nasa.gov/, https://www.mpe.mpg.de/jcg/grbgen.html, and the official *Swift* website https://swift.gsfc.nasa.gov/results/batgrbcat/.

DATA AVAILABILITY

The corresponding author will share all other data underlying this paper on reasonable request.

REFERENCES

Abbott B. P. et al., 2017, Phys. Rev. Lett., 119, 161101
Abramovici A. et al., 1992, Science, 256, 325
Amati L., 2005, Il Nuovo Cimento C, 28, 251
Amati L., 2006, MNRAS, 372, 233
Amati L., Della Valle M., 2013, Int. J. Mod. Phys. D, 22, 1330028
Amati L. et al., 2002, A&A, 390, 81
Ando S., 2004, J. Cosmol. Astropart. Phys., 06, 007
Band D. L., Preece R. D., 2005, ApJ, 627, 319
Band D. et al., 1993, ApJ, 413, 281
Belczynski K., Kalogera V., Bulik T., 2002, ApJ, 572, 407
Bucciantini N., Metzger B. D., Thompson T. A., Quataert E., 2012, MNRAS, 419, 1537
Burgess J. M., 2014, MNRAS, 445, 2589
Burrows D. N. et al., 2005, Science, 309, 1833
Butler N. R., Bloom J. S., Poznanski D., 2010, ApJ, 711, 495
Cao X.-F., Yu Y.-W., Cheng K. S., Zheng X.-P., 2011, MNRAS, 416, 2174
Chang X.-Z., Lü H.-J., Yang X., Chen J.-M., Liang E.-W., 2023, ApJ, 943, 146
Connaughton V., 2002, ApJ, 567, 1028
Coward D., 2007, New Astron. Rev., 51, 539
Daigne F., Mochkovitch R., 1998, MNRAS, 296, 275
Dainotti M. G., Petrosian V., Bowden L., 2021, ApJ, 914, L40
Demianski M., Piedipalumbo E., Sawant D., Amati L., 2017a, A&A, 598, A112
Demianski M., Piedipalumbo E., Sawant D., Amati L., 2017b, A&A, 598, A113
Deng C.-M., Wang X.-G., Guo B.-B., Lu R.-J., Wang Y.-Z., Wei J.-J., Wu X.-F., Liang E.-W., 2016, ApJ, 820, 66
Deng C.-M., Wei J.-J., Wu X.-F., 2019, J. High Energy Astrophys., 23, 1
Deng Q. et al., 2022, ApJ, 940, 5
Dermer C. D., 2007, ApJ, 659, 958
Desai D., Metzger B. D., Foucart F., 2019, MNRAS, 485, 4404
Dong X. F., Li X. J., Zhang Z. B., Zhang X. L., 2022, MNRAS, 513, 1078
Dong X. F., Zhang Z. B., Li Q. M., Huang Y. F., Bian K., 2023, ApJ, 958, 37
Efron B., Petrosian V., 1992, ApJ, 399, 345
Fenimore E. E., Ramirez-Ruiz E., 2000, preprint (arXiv:astro-ph/0004176)
Fryer C. L., Woosley S. E., Hartmann D. H., 1999, ApJ, 526, 152
Gehrels N., 1986, ApJ, 303, 336
Gehrels N. et al., 2006, Nature, 444, 1044
Gehrels N., Ramirez-Ruiz E., Fox D. B., 2009, ARA&A, 47, 567
Gruber D. et al., 2014, ApJS, 211, 12
Heussaff V., Atteia J. L., Zolnierowski Y., 2013, A&A, 557, A100
Hjorth J., 2012, PoS, GRB 2012, 136
Hjorth J. et al., 2003, Nature, 423, 847
Hopkins A. M., Beacom J. F., 2006, ApJ, 651, 142
Kaneko Y., Bostancı Z. F., Göğüş E., Lin L., 2015, MNRAS, 452, 824
Kobayashi S., Piran T., Sari R., 1997, ApJ, 490, 92
Kouveliotou C., Meegan C. A., Fishman G. J., Bhat N. P., Briggs M. S., Koshut T. M., Paciesas W. S., Pendleton G. N., 1993, ApJ, 413, L101
Krimm H. A. et al., 2009, ApJ, 704, 1405
Lan G.-X., Zeng H.-D., Wei J.-J., Wu X.-F., 2019, MNRAS, 488, 4607
Lan L., Lu R.-J., Lü H.-J., Shen J., Rice J., Li L., Liang E.-W., 2020, MNRAS, 492, 3622
Lazzati D., Ramirez-Ruiz E., Ghisellini G., 2001, A&A, 379, L39
Li Y., Zhang B., Yuan Q., 2020, ApJ, 897, 154
Li Q. M., Zhang Z. B., Han X. L., Zhang K. J., Xia X. L., Hao C. T., 2023, MNRAS, 524, 1096
Lipunov V. M., Postnov K. A., Prokhorov M. E., Panchenko I. E., Jorgensen H. E., 1995, ApJ, 454, 593
Liu Z.-Y., Zhang F.-W., Zhu S.-Y., 2021, Res. Astron. Astrophys., 21, 254
Lynden-Bell D., 1971, MNRAS, 155, 95
Mazets E. P., Aptekar R. L., Frederiks D. D., Golenetskii S. V., Il'inskii V. N., Palshin V. D., Cline T. L., Butterworth P. S., 2002, preprint (arXiv:astro-ph/0209219)
Metzger B. D., Quataert E., Thompson T. A., 2008, MNRAS, 385, 1455
Minaev P. Y., Pozanenko A. S., 2020, MNRAS, 492, 1919
Narayan R., Paczynski B., Piran T., 1992, ApJ, 395, L83
Norris J. P., Bonnell J. T., 2006, ApJ, 643, 266
Norris J. P., Marani G. F., Bonnell J. T., 2000, ApJ, 534, 248
Norris J. P., Gehrels N., Scargle J. D., 2010, ApJ, 717, 411
Palmerio J. T., Daigne F., 2021, A&A, 649, A166
Pescalli A. et al., 2016, A&A, 587, A40
Piran T., 1999, Phys. Rep., 314, 575
Qin Y.-P., Chen Z.-F., 2013, MNRAS, 430, 163
Rastinejad J. C. et al., 2022, Nature, 612, 223
Rossi A. et al., 2018, GCN Circ., 22763, 1
Sakamoto T. et al., 2008, ApJS, 175, 179
Scargle J. D., Norris J. P., Jackson B., Chiang J., 2013, ApJ, 764, 167
Singal J., Petrosian V., Lawrence A., Stawarz Ł., 2011, ApJ, 743, 104
Stanek K. Z. et al., 2003, ApJ, 591, L17
Sun H., Zhang B., Li Z., 2015, ApJ, 812, 33
van Putten M. H. P. M., Lee G. M., Della Valle M., Amati L., Levinson A., 2014, MNRAS, 444, L58
von Kienlin A. et al., 2019, ApJ, 876, 89
Wanderman D., Piran T., 2015, MNRAS, 448, 3026
Wang F. Y., Dai Z. G., 2009, MNRAS, 400, L10
Yang J. et al., 2022, Nature, 612, 232
Yonetoku D., Murakami T., Nakamura T., Yamazaki R., Inoue A. K., Ioka K., 2004, ApJ, 609, 935
Yonetoku D., Nakamura T., Sawano T., Takahashi K., Toyanago A., 2014, ApJ, 789, 65
Yu H., Wang F. Y., Dai Z. G., Cheng K. S., 2015, ApJS, 218, 13
Zeng H., Petrosian V., Yi T., 2021, ApJ, 913, 120
Zhang B., 2007, Chin. J. Astron. Astrophys., 7, 1
Zhang G. Q., Wang F. Y., 2018, ApJ, 852, 1
Zhang B. et al., 2009, ApJ, 703, 1696

Zhang Z. B., Zhang C. T., Zhao Y. X., Luo J. J., Jiang L. Y., Wang X. L., Han X. L., Terheide R. K., 2018, PASP, 130, 054202
Zhang X.-L., Zhang C.-T., Li X.-J., Su F.-F., Dong X.-F., Chang H.-Y., Zhang Z.-B., 2020a, Res. Astron. Astrophys., 20, 201
Zhang Z. B., Jiang M., Zhang Y., Zhang K., Li X. J., Zhang Q., 2020b, ApJ, 902, 40
Zhu S.-Y., Liu Z.-Y., Shi Y.-R., Ding X.-K., Sun W.-P., Zhang F.-W., 2023, ApJ, 950, 30

This paper has been typeset from a TEX/LATEX file prepared by the author.